

Full Length Article

Experimental study and DFT+U calculations on the impact of Rare-Earth ion (La^{3+} , Sm^{3+} , Y^{3+} , Yb^{3+}) doped CeO_2 Core-Shell abrasives on polishing performance



Xiaodong An^a, Jilin Wang^{a,b}, Xin Tang^a, Wenliang Chen^a, Wenke Guan^a, Changyu Liu^a, Daijiang Peng^{a,c,*}

^a School of Materials Science and Engineering, Guilin University of Technology, Guilin 541004, China

^b Guangxi Key Laboratory of Optical and Electronic Materials and Devices, Collaborative Innovation Center for Exploration of Nonferrous Metal Deposits and Efficient Utilization of Resources, School of Materials Science and Engineering, Guilin University of Technology, Guilin 541004, China

^c Key Laboratory of Gems and Mineral Functional Materials (Guilin University of Technology), Education Department of Guangxi Zhuang Autonomous Region, Guilin 541004, China

ARTICLE INFO

Keywords:

CMP
Rare-Earth ion-doped
DFT+U calculations

ABSTRACT

A series of carbon spheres coated with Rare-Earth ion-doped (La^{3+} , Sm^{3+} , Y^{3+} , Yb^{3+}) CeO_2 (CS@ CeO_2) were synthesized using eco-friendly hydrothermal and chemical precipitation methods. The structural characteristics of the abrasives were thoroughly analyzed using XRD, SEM, TEM, and FT-IR techniques. A detailed analysis of Ce^{3+} and Vo concentrations on the CeO_2 layer surface was conducted using XPS and Raman spectroscopy. The analysis results indicated that CS@ $\text{Ce}_{0.9}\text{Y}_{0.1}\text{O}_2$ abrasives exhibited the highest Ce^{3+} (46.23 %) and Vo (25.39 %) concentrations. Additionally, the polishing performance of the abrasives was evaluated using atomic force microscopy (AFM). The CS@ $\text{Ce}_{0.9}\text{Y}_{0.1}\text{O}_2$ abrasive exhibited superior polishing performance, achieving the lowest surface roughness ($\text{Ra} = 0.26 \text{ nm}$) compared to commercial abrasives ($\text{Ra} = 0.77 \text{ nm}$), reducing Ra by 66.23 %. Moreover, density functional theory with the Hubbard U method (DFT+U) was used to systematically investigate the oxygen vacancy formation energy, structural stability, and electronic properties of CeO_2 doped with Rare-Earth ions. These findings demonstrate that doping with Rare-Earth ions possessing ionic radii close to that of Ce^{4+} effectively enhances the concentration of oxygen vacancies and Ce^{3+} ions, which is crucial for improving polishing performance. This work provides valuable reference data on the doping of Rare-Earth ions in CeO_2 -based polishing abrasives.

1. Introduction

With advancing integrated circuit manufacturing technology, the precision requirements for planarizing semiconductor materials have consistently increased [1]. Consequently, developing advanced Chemical Mechanical Polishing (CMP) processes has become essential [2]. The effectiveness of CMP depends on the development and application of abrasives with high polishing rates, excellent flatness, and high selectivity, among which metal oxide nanoparticles (such as SiO_2 [3], CeO_2 [4], and Al_2O_3 [5]) are widely used. Compared to abrasives like SiO_2 and Al_2O_3 , which rely solely on mechanical interactions for material removal [6], CeO_2 exhibits a unique chemical tooth effect when polishing silicon-based materials, such as silicon dioxide and silicon

nitride, resulting in superior polishing quality [7]. Furthermore, cerium is abundant, inexpensive, and easy to process, simplifying the preparation of CeO_2 and promoting its application as an abrasive in CMP processes [8].

Research shows that Ce^{3+} ions in CeO_2 enhance chemical reactivity, facilitating the cleavage of Si-O bonds during the CMP process [9]. Consequently, numerous studies have aimed to increase the concentration of Ce^{3+} [10–13]. Fan et al.[14] synthesized CeO_2 nanomaterials doped with La^{3+} , Nd^{3+} , and Eu^{3+} ions using an oil-bath method. Following doping, the Ce^{3+} concentration increased from 49 % to 56 %. The material removal rate ($174.3 \pm 7.6 \text{ nm/min}$) and surface roughness ($\text{Ra} = 0.36 \pm 0.05 \text{ nm}$) both improved. Ma et al.[15] synthesized a series of $\text{Ce}_{1-x}\text{M}_x\text{O}_2$ with varying dopant types and amounts using the molten

* Corresponding author.

E-mail address: pdj@glut.edu.cn (D. Peng).

salt method, finding that doping significantly improved abrasive efficiency. The material removal rate (MRR) of CeO_2 abrasives doped with Y^{3+} , La^{3+} , and Pr^{3+} increased by 56 %, 40 %, and 44 %, respectively. Ion doping is clearly an effective method to enhance Ce^{3+} concentration, and the underlying mechanism has garnered significant research attention. Han et al. [16] systematically studied the electronic properties and defect chemistry of Gd-doped CeO_2 using density functional theory (DFT). They found that Gd-VO-Gd cluster formation has minimal impact on the defect chemistry of oxygen vacancies, and Gd doping effectively lowers oxygen vacancy formation energy. However, examining the effect of a single dopant on oxygen vacancy formation energy is not particularly decisive for selecting an appropriate dopant. Liu et al. [17] used hybrid density functional theory (DFT) calculations to systematically investigate oxygen vacancy formation energy and its influence on the electronic properties of transition metal-doped CeO_2 . The results indicate that dopants causing minimal structural distortion and ionic charge variation tend to bind more effectively with CeO_2 and exhibit lower oxygen vacancy formation energy. On the flip side, traditional CeO_2 abrasives relying solely on simple chemical modification often exhibit uncontrolled morphology and size, leading to mechanical damage (e.g., scratches and secondary damage) during material removal, significantly constraining their utility in CMP processes [18]. Recently, core-shell structured abrasives have been introduced to CMP to address this issue [19–22]. Kou et al. [23] successfully synthesized an $\text{mSiO}_2/\text{CeO}_2$ polishing system that significantly enhances surface quality while maintaining a high removal rate. However, the high elastic modulus of the inorganic core restricts its deformability, limiting the contact area with the polishing interface and ultimately constraining the enhancement of polishing performance [24]. As a result, organic cores with narrow size distributions and low elastic moduli have garnered significant attention from researchers. During polishing, the spring effect of the core efficiently enhances the contact area between the abrasive and the workpiece. Li et al. [25] successfully synthesized a Rare-Earth ion-doped core-shell structure, $\text{PS}@\text{CeO}_2$, via a low-temperature, two-step method, exhibiting exceptional glass polishing performance with an MRR of 480.22 nm/min and a Ra of 0.32 nm. Nevertheless, the synthesis of organic cores may release harmful substances, and the connection between most organic cores and the surface layer is merely a simple physical attachment. Additionally, the selection of Rare-Earth ions is highly diverse. Therefore, further adoption of eco-friendly processes for organic core synthesis and optimization of rare earth ion doping strategies are critically needed.

In this work, a series of $\text{CS}@\text{CeO}_2$ abrasives doped with Rare-Earth ions (La^{3+} , Sm^{3+} , Y^{3+} , Yb^{3+}) were prepared using simple hydrothermal and chemical precipitation methods. The effect of Rare-Earth ion doping on the surface chemical activity of CeO_2 was explored. A comprehensive analysis was conducted to systematically discuss the correlation between the radii of Rare-Earth ions and Vo formation energy, leveraging DFT+U calculations and experimental characterizations. Additionally, a quantitative analysis was conducted to investigate the formation mechanisms of Ce^{3+} and Vo within CeO_2 crystals and to assess their impact on CMP performance. Furthermore, the CMP mechanism of core-shell abrasives was thoroughly investigated. Compared to commercial abrasives, the optimized abrasive $\text{CS}@\text{Ce}_{0.9}\text{Y}_{0.1}\text{O}_2$ demonstrated a remarkable 66.23 % reduction in the surface roughness of the polished material. This work offers novel insights for future Rare-Earth ion-doped CeO_2 systems.

2. Experiment

2.1. Materials

D(+) Glucose monohydrate ($\text{C}_6\text{H}_{12}\text{O}_6 \cdot \text{H}_2\text{O}$, ≥ 99.5 %); urea ($\text{CO}(\text{NH}_2)_2$, ≥ 99.5 %); cerium nitrate hexahydrate ($\text{Ce}(\text{NO}_3)_3 \cdot 6\text{H}_2\text{O}$, ≥ 99.5 %), lanthanum nitrate hexahydrate ($\text{La}(\text{NO}_3)_3 \cdot 6\text{H}_2\text{O}$, ≥ 99.5 %), samarium nitrate hexahydrate ($\text{Sm}(\text{NO}_3)_3 \cdot 6\text{H}_2\text{O}$, ≥ 99.5 %), yttrium

nitrate hexahydrate ($\text{Y}(\text{NO}_3)_3 \cdot 6\text{H}_2\text{O}$, ≥ 99.5 %), ytterbium nitrate hexahydrate ($\text{Yb}(\text{NO}_3)_3 \cdot 6\text{H}_2\text{O}$, ≥ 99.5 %), and deionized water. All chemicals were of analytical grade and used without further purification.

2.2. Preparation of $\text{CS}@\text{CeO}_2$ abrasives

Polydisperse CS particles of various sizes were synthesized through a one-pot hydrothermal method in the presence of glucose as the carbon source, as reported in [26]. For a typical synthesis, 8–10 g of glucose was dissolved in 60 g of deionized (DI) water within a 100 mL Teflon-lined autoclave. Once the glucose was completely dissolved, the autoclave was placed in a preheated oven and maintained at 180 °C for up to 3 h, followed by cooling to room temperature.

The resulting dark grey suspension containing CS particles (50 g) was ultrasonicated in deionized water for 10 min. Subsequently, 0.7812 g of $\text{Ce}(\text{NO}_3)_3 \cdot 6\text{H}_2\text{O}$, 0.07 g of $\text{La}(\text{NO}_3)_3 \cdot 6\text{H}_2\text{O}$, and 10.40 g of urea (dissolved in 50 g of DI water) were added. The molar ratio of $\text{La}/(\text{Ce} + \text{La})$ in the La^{3+} -doped CeO_2 solid solution was maintained at 0.1 in this synthesis. The mixture was then slowly heated to 90 °C in an oil bath and allowed to react under magnetic stirring at 300 rpm for 3 h. The product was purified through repeated ultrasonic centrifugation, washed thoroughly with DI water and ethanol, dried overnight at 60 °C, and finally calcined at 550 °C in a nitrogen atmosphere for 4 h. Core-shell abrasives doped with different rare-earth ions were synthesized using an identical procedure.

2.3. Characterization of the abrasives

The doping element contents were measured using an inductively coupled plasma mass spectrometer (ICP-OES-Optima 8000.) The phase and crystal structure of all abrasives were analyzed using X-ray diffraction (XRD, X'Pert PRO) with $\text{Cu K}\alpha$ radiation in the scan range of 20°~80° at a scan rate of 2°/min. The microstructure was analyzed by a scanning electron microscope (SEM, S-4800, Hitachi). High-resolution transmission electron microscopy (TEM, JEM-2100) equipped with an energy dispersive spectroscopy (EDS) system was adopted to visualize the abrasives' core-shell morphology, lattice information, and element distribution. Raman spectra were collected by using a Laser Microscopic Confocal Raman Spectrometer (Thermo Fisher Scientific DXR) with a 532 nm laser as the excitation source. X-ray photoelectron spectroscopy (XPS) spectra were obtained using an ESCALAB 250Xi spectrometer with $\text{Al K}\alpha$ radiation ($h\nu = 1486.6$ eV). Chemical bonding information of the abrasives was carried out with Fourier transform infrared spectroscopy (FT-IR, Avatar 670, Nicolet).

2.4. Density functional theory (DFT) calculation

Density functional theory (DFT) [27] calculations were performed using the Vienna Ab initio Simulation Package (VASP) [28]. The projector-augmented wave (PAW) method was utilized to describe the electron-ion interactions. The exchange-correlation interaction functional is treated with the generalized gradient approximation (GGA) in the Perdew-Burke-Ernzerhof (PBE) functional [27,29]. The electronic wave functions were expanded using plane waves with an energy cutoff of 500 eV. An effective Hubbard parameter U was used to account for the strong on-site Coulomb interactions between the localized 4f orbitals of lanthanides, with U parameters set to 5 eV for $\text{Ce}4f$ and 5.5 eV for $\text{O}2p$ states respectively [15]. The convergence for total energy and the forces between atoms were set to 10^{-5} eV and $0.01 \text{ eV} \cdot \text{\AA}^{-1}$, respectively. A G-centered Monkhorst-Pack k-point mesh with a size of $2 \times 2 \times 2$ was applied [16,30]. The conjugate gradient algorithm was employed to fully relax all atomic positions.

Research suggests that doping two atoms and introducing an oxygen vacancy in a 1NN position, relative to the doped atoms, is the most energetically favorable scenario [31]. The model utilized in this work is

depicted in Fig.S1(a-c). The molecular compositions of the models are as follows: Ce₃₂O₆₄, Ce₃₀La₂O₆₄, Ce₃₀Sm₂O₆₄, Ce₃₀Y₂O₆₄, Ce₃₀Yb₂O₆₄, which correspond to CeO₂, La-CeO₂, Sm-CeO₂, Y-CeO₂, Yb-CeO₂, respectively.

2.5. CMP experiment

The abrasive was dispersed through grinding, with the solid content in the slurry adjusted to 0.5 wt%, and the pH value of the slurry was adjusted to 10.0 using a 0.1 mol/L Na₂CO₃ solution. The quartz glass, with a nominal diameter of 20 mm and a thickness of 2 mm, was purchased from Donghai Yibo Quartz Products Co., Ltd. (China) as the polishing substrate. The commercial abrasive (simple) was purchased from Dongguan Zhongwei Grinding Technology Co., Ltd. The CMP experiments were performed on a UNIPOL-1200S automatic pressure polishing machine (China Shenyang Kejing Instrument Co., Ltd.), equipped with a polyurethane polishing pad (China Shenyang Kejing Instrument Co., Ltd.). The specific polishing parameters were as follows: the rotation speeds of the polishing disc and the sample holder plate were 60 rpm, rotating in opposite directions, the polishing load was 3.0 kg, and the polishing time was 4 min. Using the SKZD-2 dropper (China Shenyang Kejing Instrument Co., Ltd.), the roller speed was 15 rpm, and the slurry supply rate was 10 mL/min. After polishing, the samples were ultrasonically cleaned repeatedly in deionized water and ethanol, dried, and then characterized for CMP performance. The surface defects and roughness of the substrates were characterized using an atomic force microscope (AFM), operating in contact mode with a scan rate of 1.0 Hz over a 5 μm × 5 μm area. For evaluating the polishing efficiency, the weight loss of the polishing workpieces was measured using a precision electronic balance with an accuracy of 0.01 mg. The material removal rate (MRR) was calculated according to Eq (1) [32].

$$MMR = \frac{m_0 - m}{\rho^* s^* t} \quad (1)$$

where ρ is the density of the glass, equal to 2.52 g/cm³ (measured using a glass density meter, MD-100, Beijing Xuhui Xinrui Technology Co., Ltd.), s is the surface area, here 1 cm², t is the polishing time and m is the weight loss. Three parallel experiments were conducted for each polishing slurry, and the arithmetic mean value was used to represent the MRR results.

3. Results and discussion

3.1. Structural analyses of abrasives

Elemental quantification was conducted using ICP-OES, as detailed in Table 1. The measured doping concentrations closely matched the nominal value (10 %), indicating effective dopant control using the precipitation method. Fig. 1 shows the XRD patterns of the doped abrasives. The characteristic diffraction peaks appear at about 28.5°, 33°, 47.5°, 56.5°, 69.5°, and 77.7°, corresponding to the (111), (200), (220), (311), (400), and (331) planes of cubic fluorite-type CeO₂, respectively. However, the peak shapes lack sharpness, indicating low crystallinity in cerium dioxide. Diffraction peaks attributed to Rare-Earth oxides (La₂O₃, Sm₂O₃, Y₂O₃, Yb₂O₃) were difficult to discern in the doped CeO₂ samples, implying effective incorporation of the doped

Rare-Earth ions into the CeO₂ matrix. Compared to pure CeO₂, the (111) peak of CS@Ce_{0.9}La_{0.1}O₂ and CS@Ce_{0.9}Sm_{0.1}O₂ doped samples shifted to lower angles. Conversely, the (111) peak of CS@Ce_{0.9}Y_{0.1}O₂ and CS@Ce_{0.9}Yb_{0.1}O₂ doped samples shifted to higher angles. The lattice parameters of the doped abrasives were determined from the broadening of the X-ray lines in the (111) diffraction using Bragg's Law Eq (2) [33] and Scherrer Eq (3) [34] equations, as shown in Table 2. The calculated lattice constants of CS@CeO₂, CS@Ce_{0.9}La_{0.1}O₂, CS@Ce_{0.9}Sm_{0.1}O₂, CS@Ce_{0.9}Y_{0.1}O₂, and CS@Ce_{0.9}Yb_{0.1}O₂ were approximately 5.413, 5.458, 5.430, 5.410, and 5.409, respectively. The introduction of La³⁺ (103.2 pm) and Sm³⁺ (95.8 pm), with ionic radii slightly larger than Ce⁴⁺ (92 pm), led to lattice expansion due to their larger lattice constants compared to pure CeO₂. Conversely, the introduction of Y³⁺ (89.9 pm) and Yb³⁺ (86.8 pm), with ionic radii slightly smaller than Ce⁴⁺, led to lattice contraction as their lattice constants were slightly smaller than that of pure CeO₂. The diffraction peaks of the doped samples show a noticeable shift compared with pristine CeO₂, suggesting that La³⁺, Sm³⁺, Y³⁺, and Yb³⁺ are doped in the lattice. No broad peak characteristic of amorphous materials (JCPDS No. 29-0085) was observed in the XRD patterns at approximately 2θ = 22°–23°, suggesting that the CeO₂ nanocrystals resided on the CS surface, resulting in a distinct core–shell structure.

$$2dsin\theta = n\lambda \quad (2)$$

$$D = K\lambda / (\beta COS\theta) \quad (3)$$

The morphology and particle size of the samples were analyzed using SEM. SEM images clearly reveal spherical samples of varying sizes, as shown in Fig. 2. The CS@CeO₂ product exhibits an average particle size of approximately 230 nm. Compared to the CS core, CS@CeO₂ abrasives retained a spherical shape and displayed a relatively rough surface. TEM images in Fig. 3 show a contrast between the edges and centers of the abrasives, indicating a distinct core–shell structure. The contrast is attributed to the amorphous material (CS) having weaker electron beam absorption compared to CeO₂. The dense CeO₂ shell has a thickness of approximately 12.5 to 18 nm, with a thin amorphous layer (1–2 nm) uniformly coating the edges. The amorphous layer on the sample surface is a potential key factor for enhancing the material removal rate (MRR) [4]. EDS mapping confirms the homogeneous distribution of doped ions and the absence of a secondary phase. As shown in Fig. 3, the interplanar spacings of the (111) plane for CS@CeO₂, CS@Ce_{0.9}La_{0.1}O₂, CS@Ce_{0.9}Sm_{0.1}O₂, CS@Ce_{0.9}Y_{0.1}O₂, and CS@Ce_{0.9}Yb_{0.1}O₂ are 0.316 nm, 0.314 nm, 0.308 nm, and 0.314 nm, respectively, consistent with the XRD results.

FT-IR characterization of CS@CeO₂ was conducted to investigate its infrared absorption properties. As shown in Fig. 4, the broad absorption band at approximately 3405.1 cm⁻¹ is attributed to the stretching vibrations of O–H bonds (hydroxyl or carbonyl groups), as reported in [14]. The C–H stretching vibrations are observed at 2923 cm⁻¹ and 2852 cm⁻¹. The absorption bands centered at approximately 1718.2 cm⁻¹ correspond to the C=O stretching vibrations of aromatic carboxyl groups (C₆H₅–C=O). The absorption band at approximately 1557.5 cm⁻¹ corresponds to C=C stretching vibrations in the aromatic carboxylic acid region, as referenced in [26]. These functional groups form during the hydrothermal process of glucose, resulting from dehydration, decarboxylation, and aromatization reactions [35]. Peaks around 1384.6 cm⁻¹, 1128.1 cm⁻¹, and 1047.1 cm⁻¹ are likely associated with Ce–O–C, indicating the formation of chemical bonds between CeO₂ and CS [36,37]. This robust interaction between the core and shell suggests stronger bonding than mere physical attachment, reducing the likelihood of shell detachment. The stretching vibrations in the range of 750–875 cm⁻¹ are assigned to out-of-plane bending vibrations of aromatic C–H [5]. The peak at 835 cm⁻¹ corresponds to bridging oxygen in Ce–O–Ce, and the absorption band around 490–500 cm⁻¹ describes the presence of Ce–O stretching modes [38,39]. The IR results are consistent with the XRD analysis.

Table 1

Nominal and Measured Doping concentration of CS@CeO₂ abrasives.

Analyte	ConcUnits	CeConcUnits	Doping concentration (%)	error range
La398.852	4.5	35.2	10.6 %	0.06
Sm359.260	1.7	12.4	10.6 %	0.06
Y371.029	1.5	12.1	10.5 %	0.05
Yb328.937	0.8	6.8	9.6 %	0.04

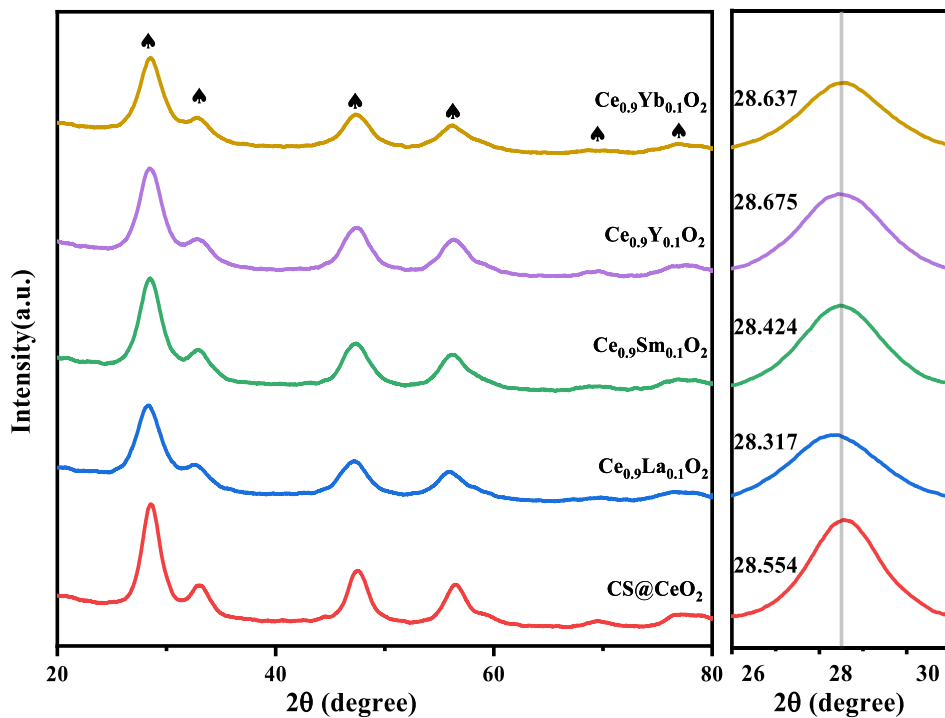


Fig. 1. XRD patterns of pure and CS@CeO₂, CS@Ce_{0.9}La_{0.1}O₂, CS@Ce_{0.9}Sm_{0.1}O₂, CS@Ce_{0.9}Y_{0.1}-O₂, CS@Ce_{0.9}Yb_{0.1}O₂.

Table 2

The data of lattice constant for CS@CeO₂, CS@Ce_{0.9}La_{0.1}O₂, CS@Ce_{0.9}Sm_{0.1}O₂, CS@Ce_{0.9}Y_{0.1}O₂, CS@Ce_{0.9}Yb_{0.1}O₂.

Type	Lattice constant (Å)	2 Theta	Crystal spacing (Å)
CS@Ce _{0.9} La _{0.1} O ₂	5.458	28.317	3.151
CS@Ce _{0.9} Sm _{0.1} O ₂	5.430	28.424	3.136
CS@Ce _{0.9} Y _{0.1} O ₂	5.410	28.675	3.124
CS@Ce _{0.9} Yb _{0.1} O ₂	5.409	28.637	3.124
CS@CeO ₂	5.413	28.554	3.125

3.2. Surface defect analysis

The Raman spectra of pure CS@CeO₂ and Rare-Earth ion-doped CS@CeO₂ hybrids are shown in Fig. 5. The D band at 1320 cm⁻¹ indicates the presence of disordered graphite structures, while the G band at 1600 cm⁻¹ signifies ordered graphite structures. The simultaneous presence of the D and G bands confirms the successful integration of CS

with CeO₂ [40,41]. The typical Raman vibrational mode (F_{2g}) associated with cubic fluorite-type CeO₂ was observed only at 440–459 cm⁻¹, with no characteristic peaks for other rare earth oxides detected [25,40]. After Rare-Earth ion doping, the F_{2g} characteristic peaks of CS@Ce_{0.9}La_{0.1}O₂ and CS@Ce_{0.9}Sm_{0.1}O₂ shifted to lower wavenumbers compared to CS@CeO₂. In contrast, the F_{2g} characteristic peak of CS@Ce_{0.9}Yb_{0.1}O₂ shifted to higher wavenumbers. Interestingly, the F_{2g} characteristic peak of CS@Ce_{0.9}Y_{0.1}O₂ shifted to lower wavenumbers, likely due to the increased concentration of Ce³⁺ [40]. The shifts in the Raman peaks provide further evidence of successful Rare-Earth ion-doping into the CeO₂ matrix, validating the preliminary findings from XRD analysis.

The peaks at 576–587 cm⁻¹ correspond to structural defects in CeO₂, primarily oxygen vacancies (V_O). The intensity ratios of the peaks at 455–459 cm⁻¹ and 576–587 cm⁻¹, denoted as I₁ and I₂, respectively, reflect the concentration of V_O due to the presence of Ce³⁺ in the CeO₂ system [40]. The calculated I₂/I₁ values for CeO₂/Air, CS@CeO₂, CS@Ce_{0.9}La_{0.1}O₂, CS@Ce_{0.9}Sm_{0.1}O₂, CS@Ce_{0.9}Y_{0.1}O₂, and CS@Ce_{0.9}Yb_{0.1}O₂ are 0.08, 0.11, 0.13, 0.12, 0.21, and 0.17,

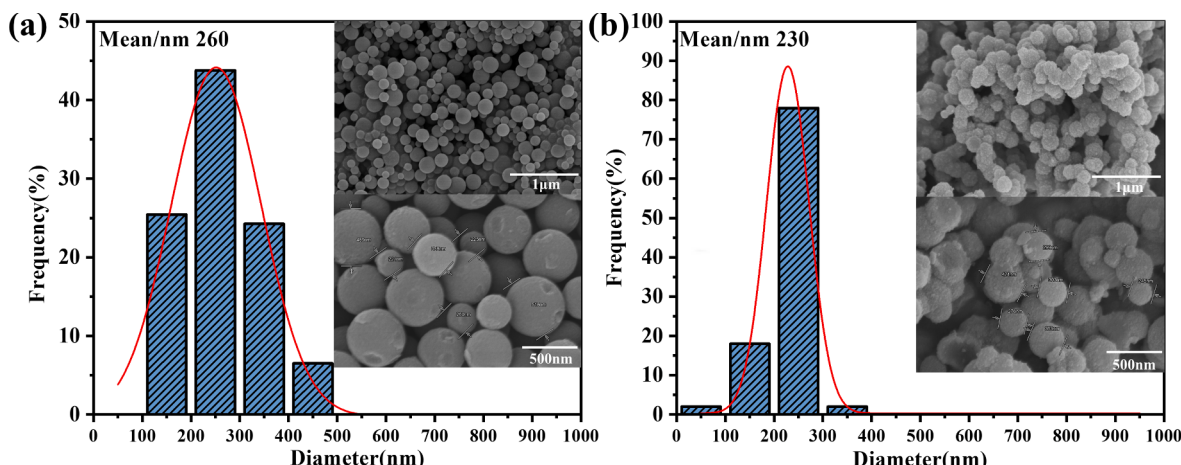


Fig. 2. SEM images of CS and CS@CeO₂.

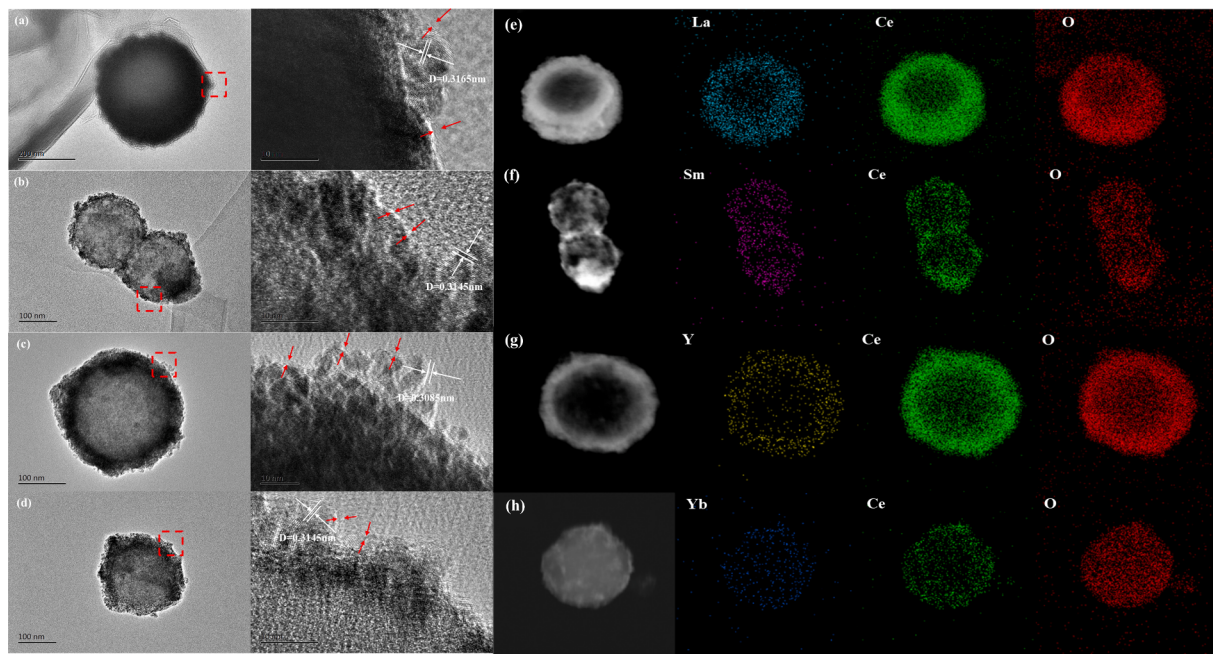


Fig. 3. HRTEM images of (a) CS@Ce_{0.9}La_{0.1}O₂ (b) CS@Ce_{0.9}Sm_{0.1}O₂ (c) CS@Ce_{0.9}Y_{0.1}O₂ (d) CS@Ce_{0.9}Yb_{0.1}O₂; Energy disperse spectroscopy (EDS) mapping images of the as-prepared nanospheres: (e) CS@Ce_{0.9}La_{0.1}O₂ (f) CS@Ce_{0.9}Sm_{0.1}O₂ (g) CS@Ce_{0.9}Y_{0.1}O₂ (h)CS@Ce_{0.9}Yb_{0.1}O₂.

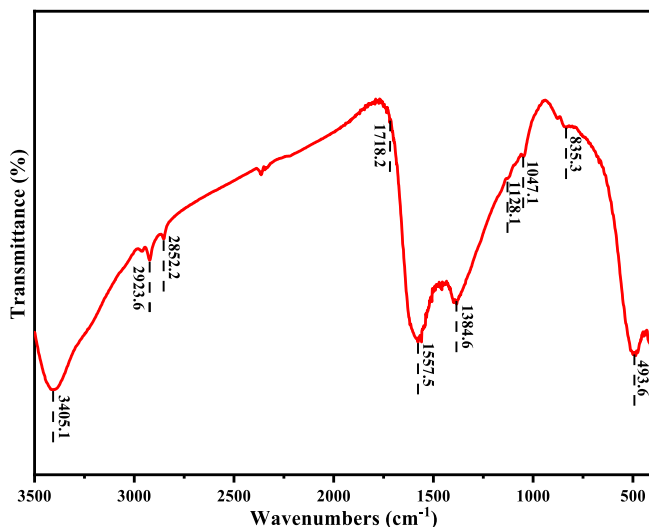


Fig. 4. FT-IR spectra of CS@CeO₂.

respectively. Notably, samples calcined in N₂ exhibit a significantly higher Vo content compared to those calcined in air, with doping further increasing the Vo content. After Y³⁺ doping, the CeO₂ lattice shows enrichment of Vo, with the highest content observed.

The shift in the F_{2g} band position is influenced by defects, strain, and grain size. The oxygen vacancy concentration N (cm⁻³) in the samples is calculated using the correlation length L (nm). The defect concentration is calculated using Eq. (4)–(6) [10].

$$\Gamma(\text{cm}^{-1}) = 5 + 51.8/d_g(\text{nm}) \quad (4)$$

$$L(\text{nm}) = \sqrt[3]{\frac{a}{2d_g}}^2 [(d_g - 2a)^3 + 4d_g^2a] \quad (5)$$

$$N = 3/4\pi L^3 \quad (6)$$

Here, Γ (cm⁻¹) is the full width at half maximum (FWHM), and a, dg,

and L represent the radius of the CeO₂ unit cell (0.34 nm), correlation length, and grain size, respectively. The calculations show that the oxygen vacancy concentration in samples calcined in N₂ is significantly higher than in those calcined in air, with CS@Ce_{0.9}Y_{0.1}O₂ exhibiting the highest oxygen vacancy concentration.

In summary, our findings demonstrate that calcination in an N₂ atmosphere, combined with Y³⁺ doping, promotes the generation of additional surface defects (Ce³⁺ and Vo), significantly enhancing tribochemical activity.

XPS spectroscopy was used to characterize the chemical bonds, surface composition, and elemental valence states of a series of CS@CeO₂ samples. The recorded XPS survey spectrum (Fig. 6(a)) shows the presence of Ce, O, and C, and specific peaks for La, Sm, Y, and Yb were identified in the CS@Ce_{0.9}La_{0.1}O₂, CS@Ce_{0.9}Sm_{0.1}O₂, CS@Ce_{0.9}Y_{0.1}O₂, and CS@Ce_{0.9}Yb_{0.1}O₂ samples, respectively. This finding further corroborates the results from EDS analysis.

The high-resolution C1s XPS spectrum (Fig. 6(b)) can be resolved into five peaks centered at 284.24, 284.74, 285.27, 286.53, and 288.93 eV [42]. The peaks at 288.93 and 286.53 eV correspond to C=C and C-C bonds. In contrast, the peaks at 285.27, 284.74, and 284.24 eV can be attributed to C-OH, C=O, and O-C=O bonds [14]. These results can be attributed to the formation of graphitic carbon (C-C, CH_x), phenolic carbonyl (C₆H₅-C=O), carbonyl, and ester groups (C=O, -COOR) during the carbonization process, which involves complex reactions such as dehydration (e.g., aldol condensation, esterification), decarbonylation, and aromatization.

The XPS spectra of O1s can be deconvoluted into three distinct peaks, as shown in Fig. 6(l-p). These peaks are centered at approximately 527.8 eV, 531.3 eV, and 532.3 eV. They correspond to O²⁻ ions in CeO₂, lattice oxygen (O₁), oxygen associated with Vo in the CeO₂ matrix (O_β), and adsorbed oxygen (O₃) [15,25]. Based on peak area ratios calculated using Eq. (7), the relative content of O_β species follows this descending order: CS@Ce_{0.9}Y_{0.1}O₂ (O_β%= 25.39 %) > CS@Ce_{0.9}Sm_{0.1}O₂ (O_β%= 21.23 %) > CS@Ce_{0.9}La_{0.1}O₂ (O_β%= 21.23 %) > CS@Ce_{0.9}Yb_{0.1}O₂ (O_β%= 17.36 %). Notably, the O_β content in all these samples is higher than in CeO₂/Air (O_β%= 15.43 %) and CS@CeO₂ (O_β%= 16.67 %).

$$\frac{\text{Vo}}{O_{\text{lattice}} + \text{Vo} + O_{\text{absorption}}} = \frac{\text{area}(O_2)}{\text{totalarea}} \quad (7)$$

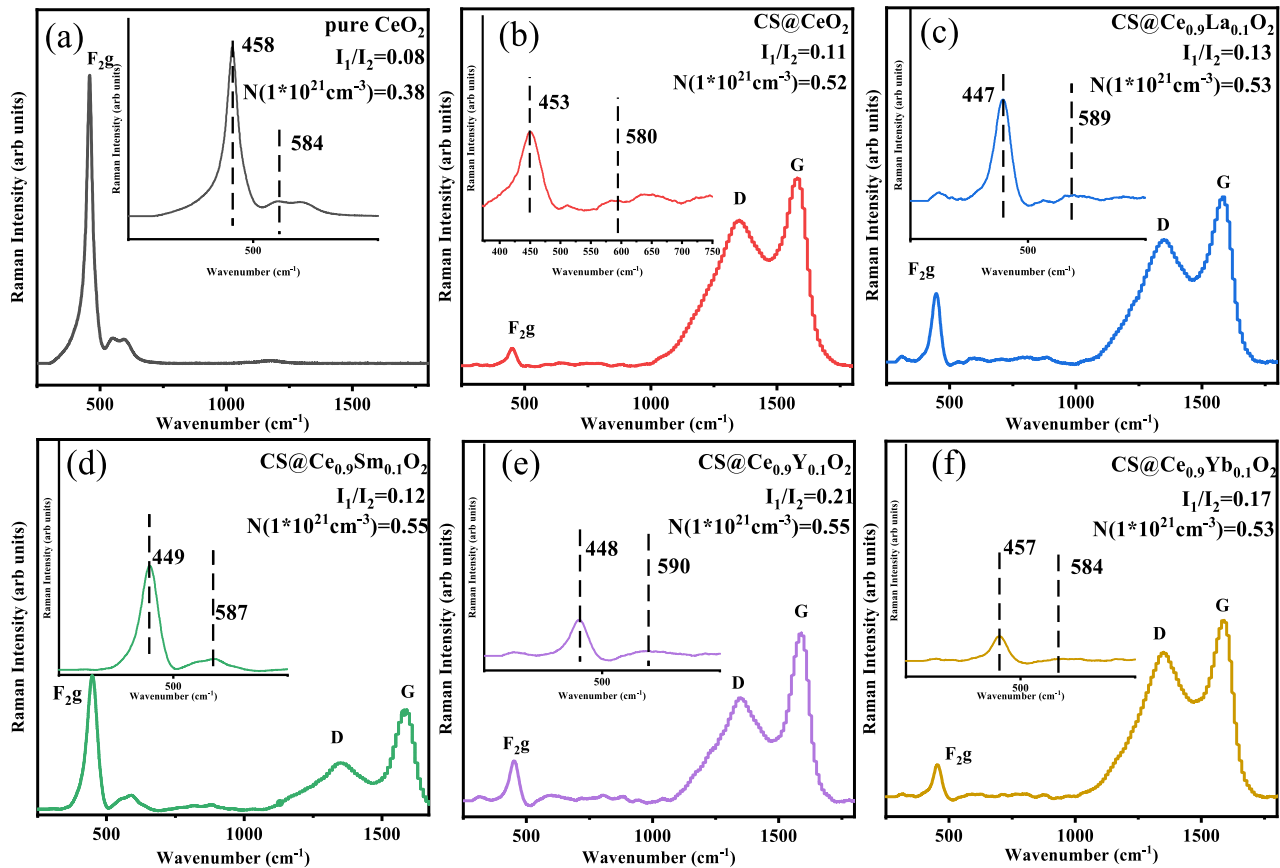


Fig. 5. Raman spectra of CeO_2/AIR , $\text{CS}@ \text{CeO}_2$, $\text{CS}@ \text{Ce}_{0.9} \text{La}_{0.1} \text{O}_2$, $\text{CS}@ \text{Ce}_{0.9} \text{Sm}_{0.1} \text{O}_2$, $\text{CS}@ \text{Ce}_{0.9} \text{Y}_{0.1} \text{O}_2$, $\text{CS}@ \text{Ce}_{0.9} \text{Yb}_{0.1} \text{O}_2$.

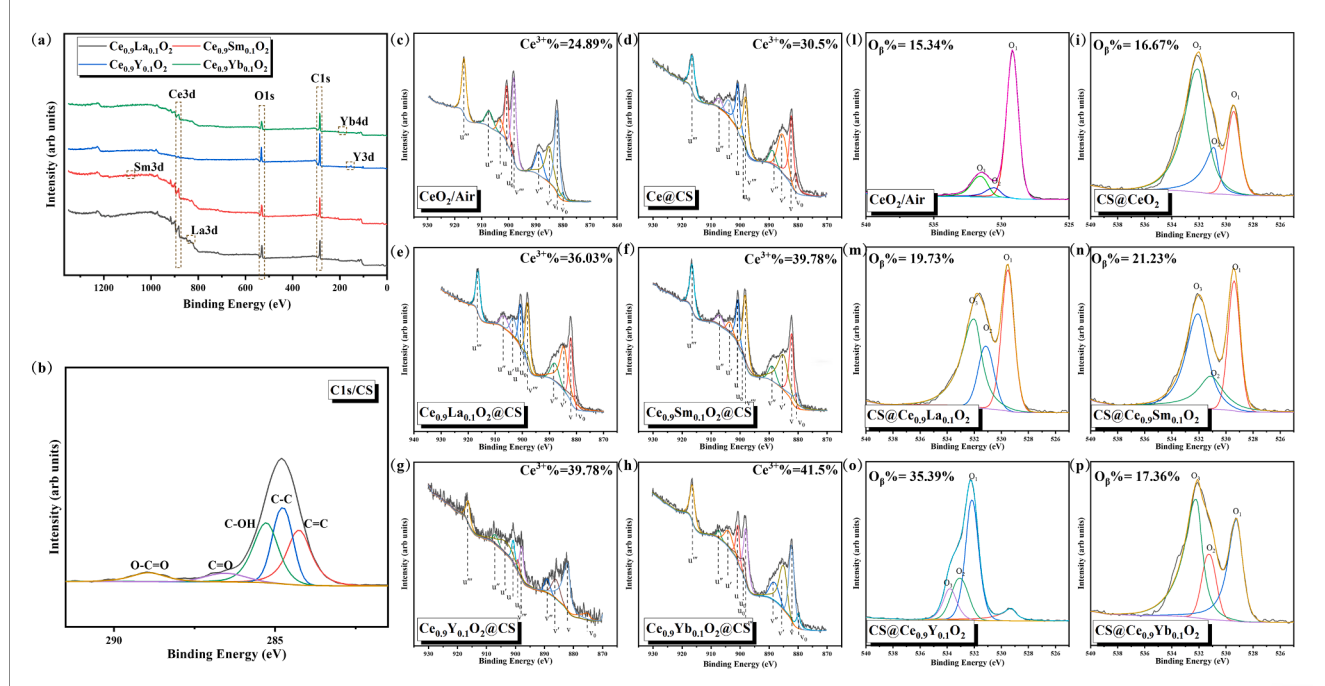


Fig. 6. (a): Survey XPS spectra of CS@Ce_{0.9}La_{0.1}O₂, CS@Ce_{0.9}Sm_{0.1}O₂, CS@Ce_{0.9}Y_{0.1}O₂, CS@Ce_{0.9}Yb_{0.1}O₂; (b) XPS spectra of C1s; XPS spectra of Ce3d(c-h) and O1s(l-p) of CeO₂/Air, CS@CeO₂, CS@Ce_{0.9}La_{0.1}O₂, CS@Ce_{0.9}Sm_{0.1}O₂, CS@Ce_{0.9}Y_{0.1}O₂, CS@Ce_{0.9}Yb_{0.1}O₂.

Fig. 6(c-h) show the Ce3d fine spectra of the samples. The Ce3d electron core level consists of two spin-orbit doublets, 3d_{3/2} and 3d_{5/2}. The Ce3d core level peaks, modulated by fluctuations in the Ce4f electron states, reflect the variations between Ce³⁺ and Ce⁴⁺. The Ce3d core level spectra were further analyzed using nonlinear peak fitting methods. The peaks corresponding to the spin-orbit 3d_{3/2} and 3d_{5/2} are labeled as u and v, respectively. The peaks labeled as v, v'', v''', u, u', and u''' represent Ce⁴⁺, while peaks labeled as v₀, v', u₀, and u' correspond to Ce³⁺. The presence of both Ce³⁺ and Ce⁴⁺ peaks across all samples indicates a mixed valence state of +3 and +4 within the CeO₂ samples. The valence state of Ce was semi-quantitatively analyzed using the peak area ratio, as described in Eq. (8) [4]. The Ce³⁺ concentration in pure CeO₂ abrasives calcined in air was 24.89 %, and for CS@CeO₂ abrasives, it rose to 30.5 %, indicating that calcination in an N₂ atmosphere enhances Ce³⁺ concentration, supporting the preliminary findings from Raman analysis. The Ce³⁺ concentrations on the surfaces of CS@Ce_{0.9}La_{0.1}O₂, CS@Ce_{0.9}Sm_{0.1}O₂, CS@Ce_{0.9}Y_{0.1}O₂, and CS@Ce_{0.9}Yb_{0.1}O₂ abrasive samples were 30.5 %, 39.78 %, 36.03 %, 46.23 %, and 41.2 %. Notably, all measured concentrations exceeded the Ce³⁺ concentration of CS@CeO₂ (30.5 %), underscoring the effectiveness of doping in enhancing the Ce³⁺ concentration.

$$\frac{Ce^{3+}}{Ce^{3+} + Ce^{4+}} = \frac{\text{area}(\nu_0, \mu_0, \nu', \mu')}{\text{totalarea}} \quad (8)$$

Analysis of the Ce3d and O1s spectra reveals that a high Ce³⁺ content strongly correlates with an elevated abundance of Vo on the surface. A clear linear relationship exists between Ce³⁺ content and Vo content.

3.3. CMP performances

High-resolution surface topography and roughness within a 5 × 5 μm² area, along with cross-sectional line-scan profiles (SR) of wafers before and after abrasive polishing, were analyzed using Atomic Force Microscopy (AFM). The limited scan rate of AFM confines the

acquisition of high-resolution images to small areas, typically ~5 × 5 μm². To reduce variability in polishing outcomes, three random measurement locations were selected on the polished plane of each sample, and their results were averaged. Profile measurements were taken diagonally across the 2D-AFM height images for comparison, while 3D-AFM slope images were used to visualize surface morphology changes resulting from CMP. The 2D-AFM height image before polishing is shown in **Fig. 8(a)**. The average Ra and RMS values were 1.619 nm and 2.836 nm. After CMP treatment with the abrasives, numerous nanoscale sharp peaks were effectively eliminated compared to the original surface. Additionally, the developed CS@CeO₂ and Rare-Earth ion-doped CS@CeO₂ abrasives (**Fig. 8(b, d-g)**) exhibited superior flatness in the polished planes, surpassing commercial precision polishing abrasives (**Fig. 8(c)**). The values of Ra, RMS, SR, and MRR for CS@CeO₂, CS@Ce_{0.9}La_{0.1}O₂, CS@Ce_{0.9}Sm_{0.1}O₂, CS@Ce_{0.9}Y_{0.1}O₂, and CS@Ce_{0.9}Yb_{0.1}O₂ are shown in **Fig. 7**. Compared to commercial abrasives, the Ra values for CS@CeO₂ and those doped with La³⁺, Sm³⁺, Y³⁺, and Yb³⁺ were reduced by 44.1 %, 41.5 %, 46.7 %, 66.23 %, and 45.45 %. The SR values were reduced by 51.9 %, 88.2 %, 65.42 %, 82.89 %, and 82.04 %. The RMS values (micro-roughness) were reduced by 40 %, 55.7 %, 50.7 %, 74.2 %, and 52.8 %, indicating a significant improvement in polishing quality with Rare-Earth element-doped. Among the Rare-Earth element-doped abrasives, CS@Ce_{0.9}Y_{0.1}O₂ exhibited the smallest Ra, RMS, and SR values, as well as the highest MRR value (221.04 nm/min). These results confirm that the developed CS@CeO₂ and Rare-Earth element-doped CS@CeO₂ abrasives can reduce surface roughness and achieve planarization at the nanoscale, demonstrating potential applications in precision polishing fields such as semiconductors.

3.4. DFT analysis

The formation of oxygen vacancies in CeO₂ is accompanied by the reduction of Ce⁴⁺ to Ce³⁺, a process closely linked to its polishing

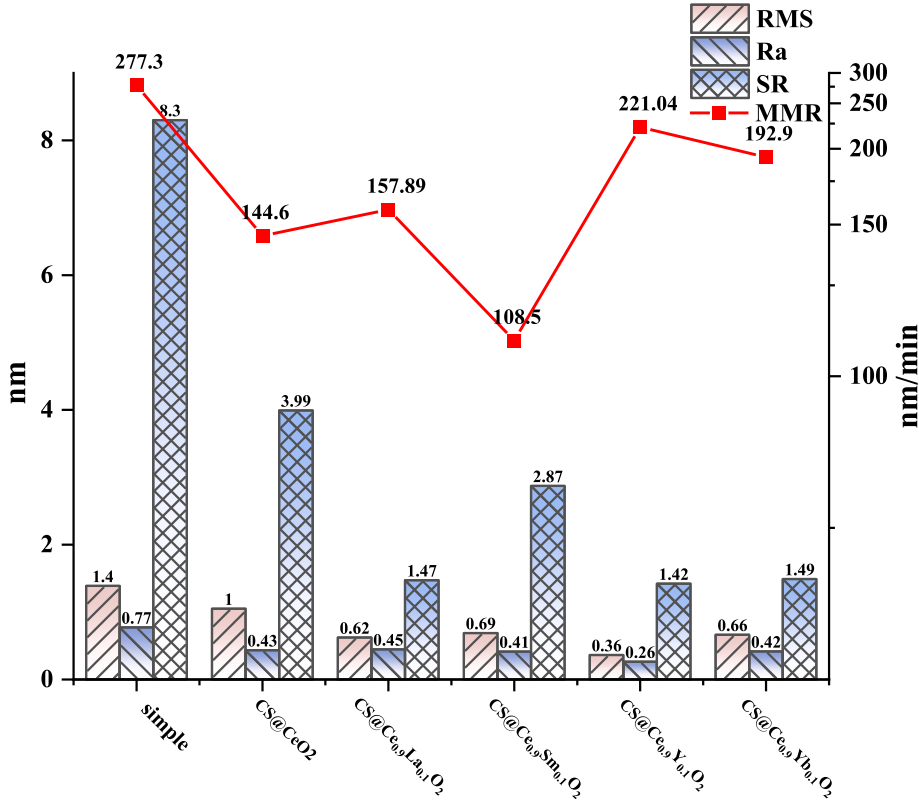


Fig. 7. RMS, Ra, SR, MMR of simple, CS@CeO₂, CS@Ce_{0.9}La_{0.1}O₂, CS@Ce_{0.9}Sm_{0.1}O₂, CS@Ce_{0.9}Y_{0.1}O₂, CS@Ce_{0.9}Yb_{0.1}O₂.

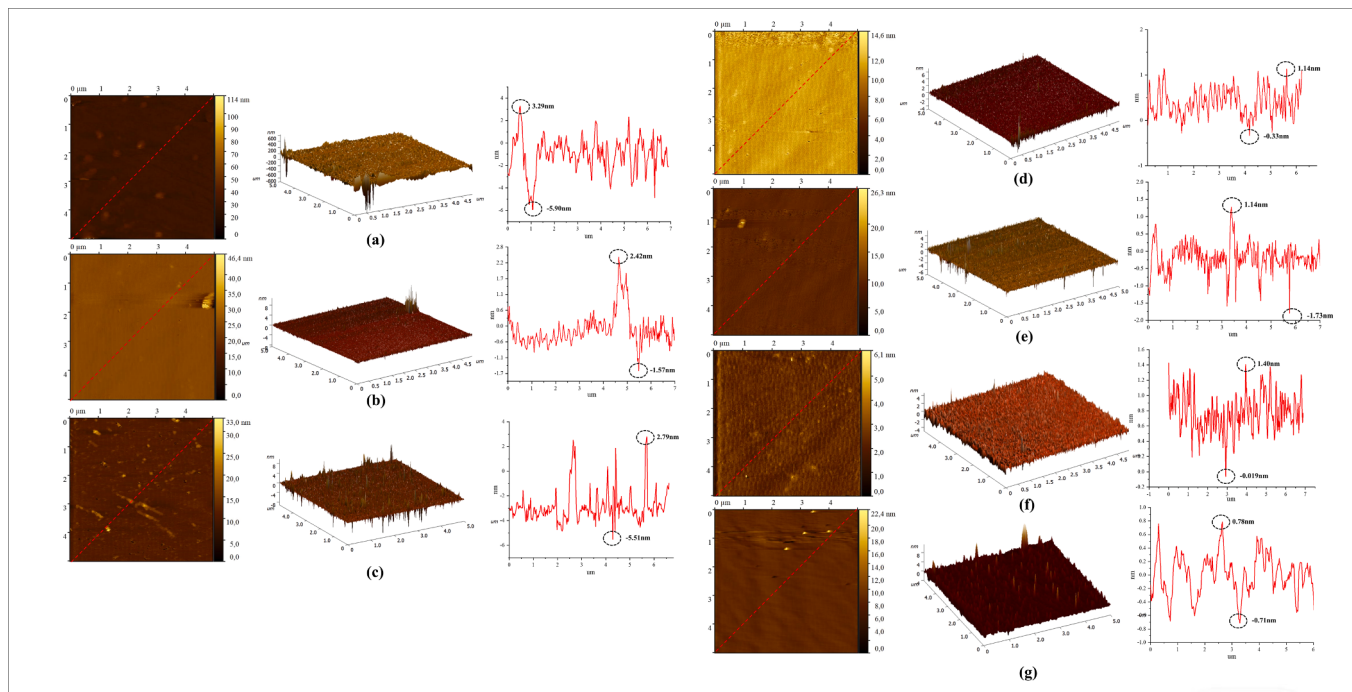


Fig. 8. 3D-, 2D-AFM images and SR of the glass substrates after CMP with (a) before polishing, (b) CS@CeO₂, (c) simple, (d) CS@Ce_{0.9}La_{0.1}O₂, (e) CS@Ce_{0.9}Sm_{0.1}O₂, (f) CS@Ce_{0.9}Y_{0.1}O₂, (g) CS@Ce_{0.9}Yb_{0.1}O₂, CS@Ce0.9Yb0.1O₂

performance. Therefore, understanding the ease of oxygen vacancy formation in CeO₂ is crucial. The impact of dopants on the formation energy of oxygen vacancies is influenced by factors such as the dopant ion's coordination number, structural relaxation, and coordination type [43–45]. In this work all dopant elements are in the “+3 valence” state, and the optimal coordination type is used to minimize the influence of coordination number and configuration.

The compensated vacancy formation energy (E_{vac}) and active oxygen vacancy formation energy (ΔE_A) of doped and undoped CeO₂ systems were analyzed and calculated using Eq. (9) [16] and Eq. (10) [17]. $E_{cell-vac}$ represents the total energy of the supercell containing oxygen vacancies, while E_{cell} corresponds to the total energy of the supercell without oxygen vacancies. Additionally, μ_0 represents the total energy of a free O₂ molecule in its ground state. $E_{(RE-doped-A)}$ denotes the energy of the doped system containing two oxygen vacancies.

$$E_{vac} = E_{cell-vac} + \mu_0 - E_{cell} \quad (9)$$

$$\Delta E_A = E_{(RE-doped-A)} + \mu_0 - E_{cell-vac} \quad (10)$$

As shown in Table 3, the E_{vac} values for the Rare-Earth ion-doped CeO₂ systems are negative, indicating that the formation of compensating oxygen vacancies under La³⁺, Sm³⁺, Y³⁺, and Yb³⁺ doping releases energy, benefiting the overall system. Among the doped CeO₂ systems, Y³⁺-doped CeO₂ exhibits the lowest E_{vac} , suggesting that, at equivalent doping concentrations, it forms the highest number of compensating oxygen vacancies. The ΔE_A values for CeO₂ systems doped with La³⁺, Sm³⁺, Y³⁺, and Yb³⁺ are all positive, indicating that energy absorption is needed to form active oxygen vacancies.

Table 3

The data of E_{vac} (ev) for CeO₂, La-CeO₂, Sm-CeO₂, Y-CeO₂, Yb-CeO₂.

Simple	$E_{(cell)}$ (ev)	$E_{(cell-vac)}$ (ev)	$E_{(RE-doped-A)}$ (ev)	E_{vac} (ev)	ΔE_A (ev)
CeO ₂	-521.53	-516.92	-513.08	3.275	2.505
La-CeO ₂	-518.51	-518.07	-513.91	-0.895	2.825
Sm-CeO ₂	-518.16	-517.74	-513.56	-0.915	2.845
Y-CeO ₂	-522.08	-521.97	-517.95	-1.225	2.685
Yb-CeO ₂	-518.54	-518.27	-514.40	-1.065	2.535

Additionally, the formation energy of active oxygen vacancies in the doped systems is higher than in the undoped CeO₂ system. This suggests that doping with La³⁺, Sm³⁺, Y³⁺, and Yb³⁺ negatively impacts the reduction of ΔE_A .

In the ideal CeO₂ structure, the electronic states near the Fermi level are mainly divided into two regions: the valence band (approximately 5 eV to 0 eV) and the conduction band (0 eV to 5 eV). Fig. 9(a) shows the partial density of states (PDOS) for the ideal CeO₂ structure. The Fig. 9(a) clearly shows that the electronic states in the valence band are primarily composed of O 2p orbitals, with some hybridization with Ce 5d and Ce 4f orbitals, resulting in a calculated bandgap of approximately 3.94 eV. The electronic states in the conduction band are primarily composed of unoccupied Ce 4f orbitals. These unoccupied Ce 4f orbitals are what give Ce⁴⁺ its unique electron storage capability. A bandgap of approximately 2.46 eV is observed between the O 2p states and Ce 4f states, consistent with findings reported in the literature [15,16,31]. Comparing the density of states (DOS) of CeO₂ before and after introducing oxygen vacancies (Fig. 9(b)) reveals the emergence of localized electronic states near the Fermi level. This occurs because the formation of an oxygen vacancy leaves behind two free electrons, which then occupy the vacant Ce 4f orbitals. Compared to the unreduced system, the DOS of the reduced system shifts to lower energy levels. This shift may be due to the localized states introduced by oxygen vacancies, located below the conduction band minimum (CBM). As a result, the electronic state density in this energy region increases, shifting the overall DOS curve to lower energies. These new states create intra-gap states near the Fermi level, narrowing the bandgap and enhancing electron transfer efficiency [46].

Comparing the DOS before and after rare-earth ion doping (Fig. 9(c-d)) shows that the bandgap of the doped system narrows (to 2.1 eV) compared to the undoped system. This bandgap reduction may result from hybridization between the dopant elements' orbitals and the Ce 4f or O 2p orbitals in CeO₂, shifting the conduction band minimum or valence band maximum towards the Fermi level. Additionally, lattice distortions and strain induced by doping may alter atomic interactions, further affecting the electronic band structure and resulting in a narrower bandgap. Fig. 9(c-d) also show that even without oxygen

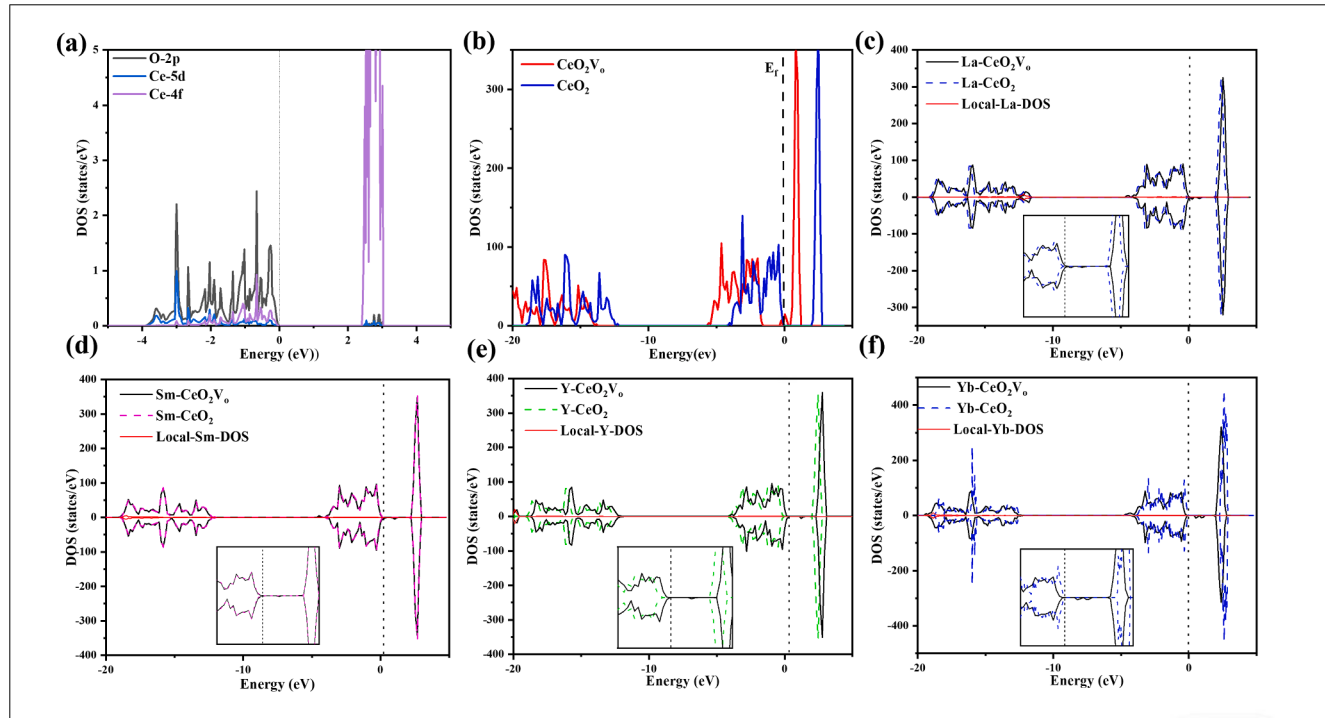


Fig. 9. PDOSS(a) for CeO_2 ; The density of states (DOS) of CeO_2 including dopants and oxygen vacancy(c-f).

vacancies, the doped systems introduce mid-gap states near the Fermi level, mainly as unoccupied states below the CBM. The appearance of these mid-gap states may be due to differences in coordination numbers between Ce^{4+} and the dopant ions in the CeO_2 matrix. However, introducing oxygen vacancies into the doped systems causes these mid-gap states to disappear. Although oxygen vacancies usually introduce two additional electrons, the DOS in Fig. 9(c-d) does not show localized states corresponding to these vacancies. Moreover, the projected density of states (PDOS) of the rare-earth ions shows no significant changes before and after introducing oxygen vacancies, indicating that the two electrons left by the vacancies do not transfer to the dopant ions or localize on the Ce 4f orbitals. Instead, they likely compensate for the hole states created by doping. Fig. 9(c-d) show that the DOS of the doped system with oxygen vacancies shifts slightly to lower energy levels compared to the system without vacancies. This slight shift may result from the formation of oxygen vacancies, leading to hybridization of the mid-gap states with the original conduction band states, thus creating new low-energy electronic states. However, the overall DOS of the doped system shows no significant changes, suggesting that it can accommodate oxygen vacancies while maintaining a relatively stable electronic structure. This suggests that changes in the electronic structure are not the primary factor driving the significant reduction in oxygen vacancy formation energy; instead, energetically favorable lattice distortions are likely the main contributors.

To investigate how structural distortions affect oxygen vacancy formation energy, the first step is to assess the impact of volume strain. The relationships between E_{vac} , ΔE_A , and volume strain after adding oxygen vacancies to the CeO_2 supercell are plotted in Fig. 10(b). For compensated oxygen vacancies, E_{vac} shows a positive correlation with volume, highlighting the critical role of volume strain. Additionally, an ionic radius closer to Ce^{4+} results in less volume change. For active oxygen vacancies, except for La-CeO_2 , a smaller ionic radius results in less volume change and lower ΔE_A . The formation enthalpy and bond lengths of the oxides are calculated and presented in Fig. 10(c). These parameters significantly impact the interactions between dopant ions and surrounding oxygen atoms. We found that ΔE_A is proportional to the bond lengths and formation enthalpy (ΔE_f) of the oxides [47]. Notably,

the bond lengths and formation enthalpy of oxides indicate the bonding ability of elements with oxygen. When an oxygen vacancy appears at a 1NN position, it significantly affects the oxygen vacancy formation energy. Fig. 10(d) shows that introducing compensated oxygen vacancies causes structural relaxation, leading to corresponding energy changes. Compared to the 4.09 eV energy change in CeO_2 , introducing oxygen vacancies in La-CeO_2 , Sm-CeO_2 , Y-CeO_2 , and Yb-CeO_2 results in additional energy changes of 0.44 eV, 0.58 eV, 0.11 eV, and 0.27 eV, respectively, indicating a substantial reduction. As the ionic radius approaches Ce^{4+} , the energy change decreases. As the ionic radius approaches Ce^{4+} , the energy change decreases.

In summary, compared to the undoped system, doping reduces structural distortions and energy fluctuations caused by oxygen vacancies. For compensated oxygen vacancies, E_{vac} decreases as the ionic radius approaches Ce^{4+} , with the Y^{3+} -doped system showing the lowest E_{vac} . For active oxygen vacancies, ΔE_A decreases as the ionic radius decreases, with the Yb^{3+} -doped system showing the lowest ΔE_A . This is likely because the influence of Rare-Earth ions with identical coordination numbers on E_{vac} primarily stems from structural distortions. Volume strain and lattice relaxation are correlated with ionic radius, where radii significantly deviating from Ce^{4+} typically result in larger geometric distortions. The lower E_{vac} of Y-CeO_2 could be due to its proximity to the Ce^{4+} radius, minimizing changes to the crystal structure upon doping and oxygen vacancy creation. The primary variations in ΔE_A energy stem from the interactions between dopant atoms and their neighboring oxygen atoms. The reduced ΔE_f and shorter bond lengths of Yb^{3+} weaken its attraction to surrounding oxygen atoms, facilitating their egress from the crystal. The absence of significant crystal structure changes upon forming active oxygen vacancies likely accounts for the reduced ΔE_A of Yb-CeO_2 .

An overall characterization reveals a correlation between the trends in oxygen vacancy concentration, Ce^{3+} concentration, and the changes in compensated oxygen vacancy formation energy. This suggests that compensated oxygen vacancies play a dominant role in the doped systems. Furthermore, the concentrations of oxygen vacancies and Ce^{3+} are related to the ionic radius. The formation energy of compensated oxygen vacancies decreases as the ionic radius approaches Ce^{4+} . Consequently,

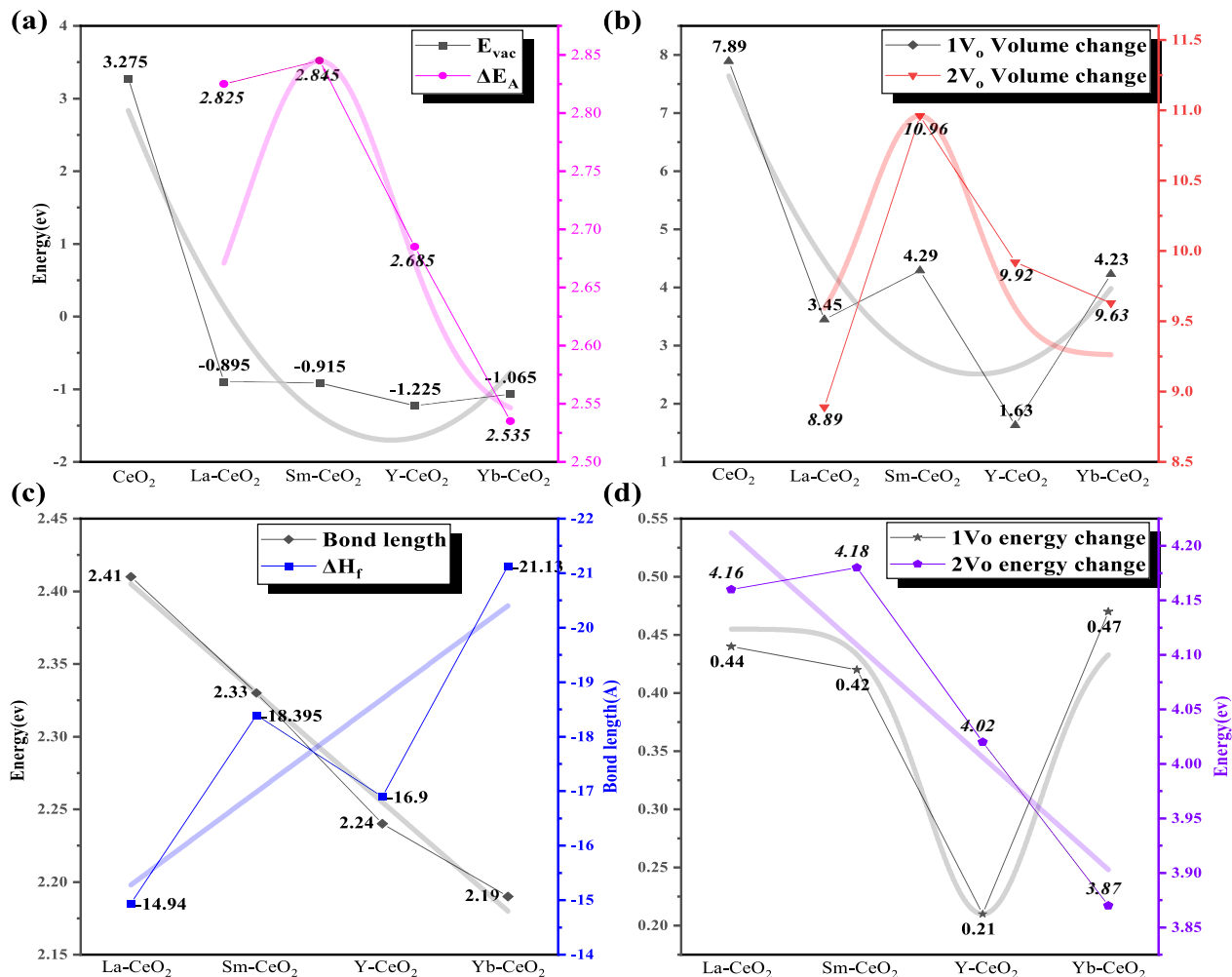


Fig. 10. ΔE_A and E_{vac} (a), the volume change of $1V_o$ and $2V_o$ (b), Re-O bond length and ΔE_f (c), $1V_o$ and $2V_o$ energy change (d) of CeO_2 and Doped rare-earth ions (La^{3+} , Sm^{3+} , Y^{3+} , Yb^{3+}).

the concentrations of oxygen vacancies and Ce^{3+} increase.

3.5. The mechanism of ion doping induced Ce^{3+} formation

Fig. 11 Shows the mechanism of ce^{3+} formation triggered by ion doping. The unique localization of Ce 4f orbitals (shown in **Fig. 11(e)**) facilitates the storage of free electrons within Ce^{4+} in the CeO_2 system. As a result, oxygen vacancies and Ce^{3+} are formed in the ceria lattice. However, forming active oxygen vacancies is challenging, significantly hindering the increase in Ce^{3+} concentration. High concentrations of oxygen vacancies can still be achieved in the CeO_2 system through doping strategies. Trivalent RE $^{3+}$ ions, as shown in **Fig. 11(a)**, are introduced into the CeO_2 lattice to replace higher-valent Ce^{4+} ions. To maintain charge balance and structural stability, lattice oxygen escapes as O_2 , as shown in **Fig. 11(b)**. This process creates oxygen vacancies and releases two free electrons to maintain charge neutrality. The electrons are captured by Ce^{4+} ions surrounding the oxygen vacancies, as shown in **Fig. 11(c)**, leading to the reduction of their oxidation state. As illustrated in **Fig. 11(d)**, the electrons are not permanently bound to any specific Ce^{4+} ion to reduce its oxidation state to + 3, but move around the vacancy under the influence of the electric field. This suggests that under certain stimuli, the electrons stored in Ce^{3+} can migrate to other locations and participate in reactions.

3.6. CMP mechanism

During the polishing process, the abrasives primarily undergo sliding and rolling motions between the substrate and the polishing pad. Polyhedral abrasives mainly rely on sliding to remove excess material, but rolling, which inevitably occurs during polishing, can cause secondary damage to the substrate due to their sharp edges. In contrast, spherical particles, due to their rounded shape, lack sharp edges and thus effectively prevent secondary damage. Moreover, spherical particles exhibit a significantly lower friction coefficient with flat substrates compared to polyhedral abrasives. As a result, spherical abrasives with low friction coefficients can effortlessly reach the top regions of crystal planes and rectangular edges, thereby enhancing polishing efficiency and debris removal.

As mentioned earlier, core-shell abrasives can effectively address the morphology issue. However, the benefits of core-shell abrasives go beyond this, offering additional advantages. Incorporating an organic core with a low elastic modulus leads to a spring-like behavior under pressure, minimizing contact stress and indentation depth while maximizing particle-surface contact area (**Fig. 12(a)**). Consequently, scratches from sliding friction are reduced, leading to improved surface quality and fewer defects [48]. Compared to commercial abrasives, core-shell abrasives exhibit smaller contact angles, resulting in superior interfacial wettability and enhanced chemical reactions at the solid-liquid interface (**Fig. S2**) [49]. Studies show a direct correlation between shell thickness and polishing amount, while surface roughness

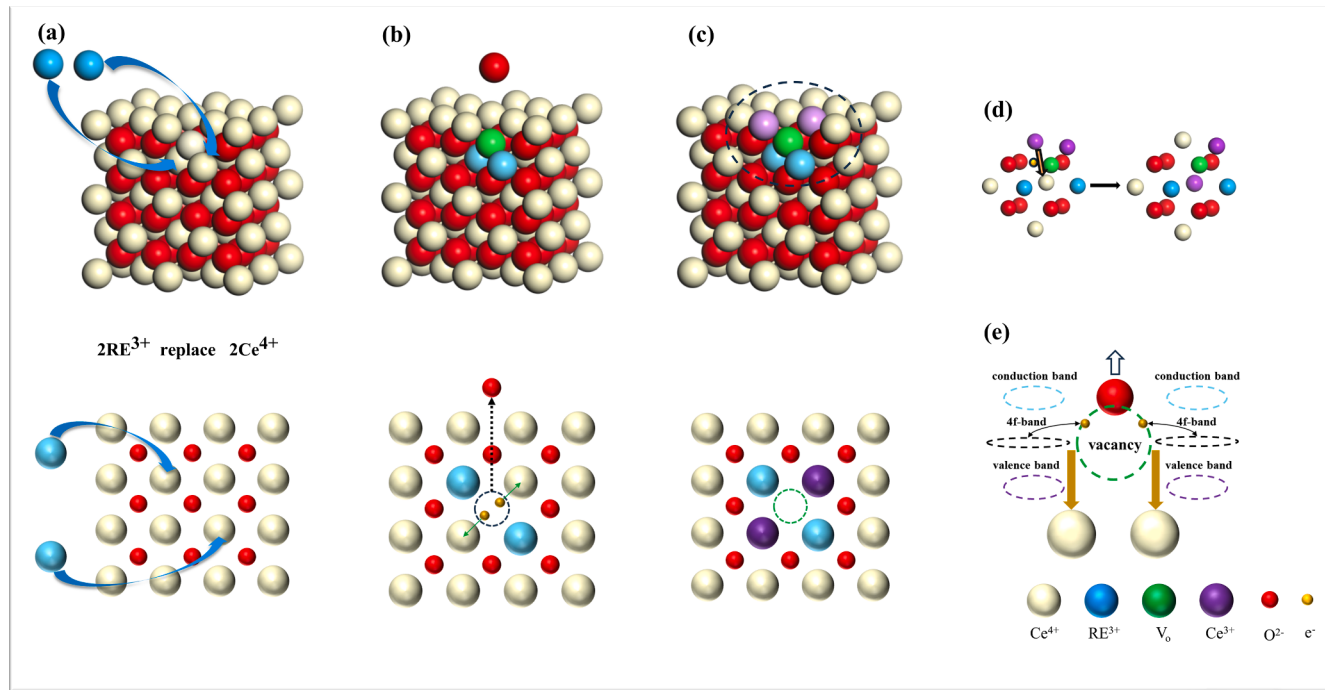


Fig. 11. Schematic diagram of the structural evolution of CeO₂ crystal doped with rare-earth ions.

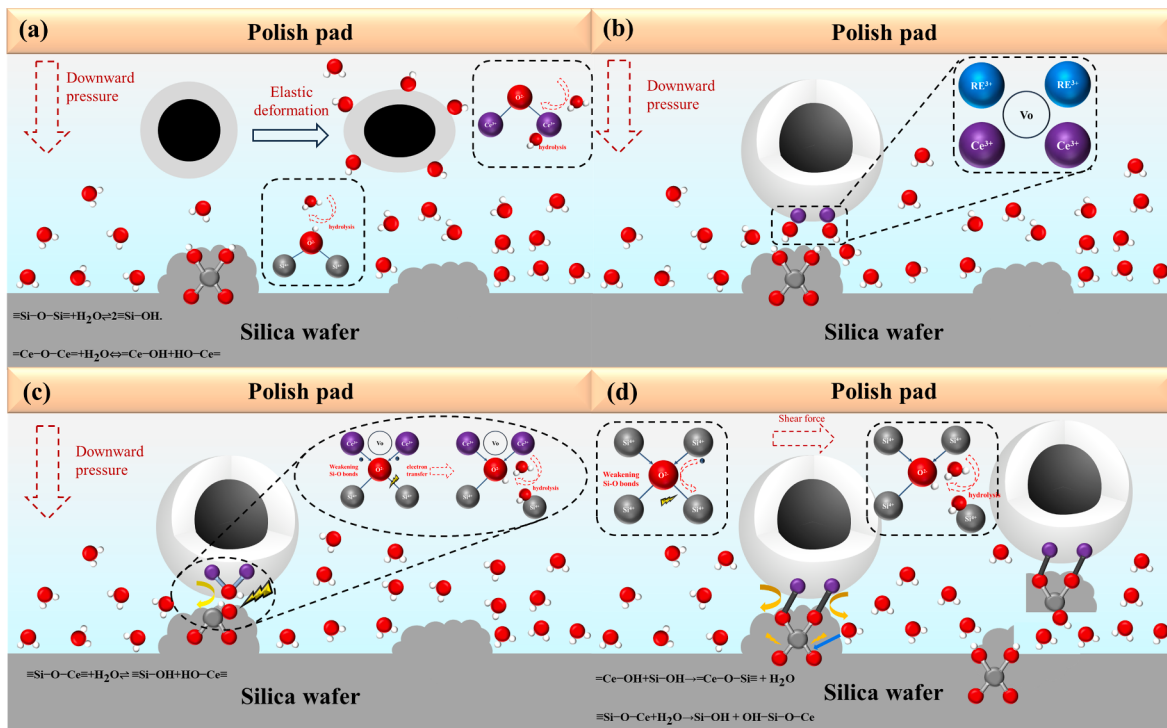


Fig. 12. Schematic diagram of the CMP mechanism for CeO₂ abrasives on SiO₂ substrate.

inversely correlates with shell thickness [50]. A shell thickness of 12–20 nm optimizes both polishing amount and quality, facilitating smaller and more uniform contact stress on the wafer surface while minimizing the risk of brittle fracture in the inorganic shell. The core-shell abrasives synthesized in this work have a surface shell thickness of 12.5–18 nm, effectively preventing shell fracture and preserving polishing quality. Additionally, the core-shell structure efficiently preserves CeO₂, resisting sedimentation and agglomeration in the polishing slurry, thus

enhancing abrasive utilization and simplifying post-polishing waste management.

Fig. 12 illustrates the polishing characteristics of cs@ceo₂ abrasives. The polishing characteristics of CeO₂ abrasives adhere to Cook's chemical tooth theory. Amphoteric oxides CeO₂ and SiO₂ undergo hydration in the slurry [51]. As shown in Fig. 12(b), the SiO₂ substrate surface hydrolyzes into hydrogen-terminated –Si-OH species, referred to as the “soft layer,” within the slurry. Under the downward pressure

exerted by the polishing machine, CeO_2 in the slurry undergoes surface hydration, leading to the formation of Ce-OH. Upon contact with the glass surface, as shown in Fig. 12(d), Ce-OH on the abrasive surface forms Ce-O-Si bonds with the Si-OH soft layer on the glass surface. Free electrons from Ce^{3+} migrate to the SiO_2 surface, entering the anti-bonding orbitals of the Si-O bonds, weakening and breaking them. Mechanical stress facilitates Si-O bond breaking, resulting in the removal of excess material from the surface. Furthermore, Fig. 12(c) shows that CeO_2 catalyzes and accelerates the chemical reaction between the glass surface and water molecules during polishing. Under the downward pressure exerted by the polishing machine, water molecules interact with Ce^{3+} ions to soften the silica surface. As Si-O bonds break, water molecules dissociate at the weakened bonds, introducing OH groups to the glass surface [52]. This process creates a softened layer on the glass surface, enabling the subsequent round of polishing. The chemical bond breakage resulting from the interaction between CeO_2 and SiO_2 significantly enhances the removal of excess material during polishing. Consequently, surface quality is significantly improved.

4. Conclusion

This work introduces a novel abrasive design concept for planarizing glass surfaces. A simple, low-temperature, and controllable two-step method was used to synthesize approximately 230 nm $\text{CS@Ce}_{0.9}\text{RE}_{0.1}\text{O}_2$ abrasives. SEM and TEM analyses revealed a thin, uniform CeO_2 layer coating polydisperse carbon spheres (CS) synthesized via a hydrothermal method, exhibiting a characteristic core-shell structure. FT-IR confirmed that CeO_2 is firmly bonded to the carbon spheres, forming strong chemical bonds. EDS, XRD, and Raman analyses confirmed the successful doping of La^{3+} , Sm^{3+} , Y^{3+} , and Yb^{3+} into the CS@CeO_2 structure. Raman and XPS results show that doping with rare earth elements increases the surface concentrations of Ce^{3+} and oxygen vacancies (V_{O}) in CeO_2 , thereby enhancing tribocatalytic activity. During the CMP process, $\text{CS@Ce}_{0.9}\text{Y}_{0.1}\text{O}_2$ abrasives exhibited excellent performance metrics ($\text{Ra} = 0.236 \text{ nm}$, $\text{RMS} = 0.361 \text{ nm}$, $\text{SR} = 1.419 \text{ nm}$, $\text{MRR} = 253.2 \text{ nm/min}$). This superior performance is attributed to enhanced tribocatalytic activity, which accelerates the removal of the chemically modified layer. DFT+U calculations revealed that in doped systems, oxygen vacancies in CeO_2 are predominantly compensatory. The concentration of oxygen vacancies and Ce^{3+} is strongly correlated with the radius of the dopant ions. The closer the ion radius is to that of Ce^{4+} , the lower the energy required to form compensatory oxygen vacancies. Consequently, the concentration of oxygen vacancies and Ce^{3+} increases. This work provides a valuable reference for optimizing Rare-Earth-doped CeO_2 CMP abrasives. It thoroughly explores the correlation between the radius of doped Rare-Earth ions and their impact on polishing performance. The findings indicate that $\text{CS@Ce}_{0.9}\text{Y}_{0.1}\text{O}_2$ exhibits excellent abrasive properties, making it a suitable candidate for high-performance CMP applications.

CRediT authorship contribution statement

Xiaodong An: Writing – review & editing, Writing – original draft, Data curation. **Jilin Wang:** Visualization, Validation. **Xin Tang:** Supervision, Software. **Wenliang Chen:** Investigation. **Wenke Guan:** Investigation. **Changyu Liu:** Investigation. **Daijiang Peng:** Writing – review & editing, Data curation, Conceptualization.

Declaration of competing interest

The authors declare that they have no known competing financial interests or personal relationships that could have appeared to influence the work reported in this paper.

Data availability

Data will be made available on request.

Appendix A. Supplementary material

Supplementary data to this article can be found online at <https://doi.org/10.1016/j.apsusc.2024.161028>.

References

- [1] J. Lee, Y. So, S. Kim, Y. Yoon, H. Rho, C. Park, Efficient integration of electro-coagulation and ceramic membranes for the treatment of real chemical mechanical polishing (CMP) slurry wastewater from the semiconductor industry, *J. Water Process Eng.* 61 (2024), <https://doi.org/10.1016/j.jwpe.2024.105326>.
- [2] H. Lee, H. Kim, H. Jeong, Approaches to sustainability in chemical mechanical polishing (CMP): a review, *Int. J. Pr. Eng. MAN-GT* 9 (2021) 349–367, <https://doi.org/10.1007/s40684-021-00406-8>.
- [3] D. Yin, X. Niu, K. Zhang, J. Wang, Y. Cui, Preparation of MgO doped colloidal SiO_2 abrasives and their chemical mechanical polishing performance on c-, r- and a-plane sapphire substrate, *Ceram. Int.* 44 (2018) 14631–14637, <https://doi.org/10.1016/j.ceramint.2018.05.087>.
- [4] L. Wang, G. Ren, W. Xie, J. Zhang, D. Pan, S. Wang, Simple and facile synthesis of single-crystal CeO_2 abrasives and its highly efficient removal mechanism on SiO_2 film, *Appl. Surf. Sci.* 654 (2024), <https://doi.org/10.1016/j.apsusc.2024.159510>.
- [5] H. Lei, N. Bu, R. Chen, P. Hao, S. Neng, X. Tu, K. Yuen, Chemical mechanical polishing of hard disk substrate with α -alumina-g-polystyrene sulfonic acid composite abrasive, *Thin Solid Films* 518 (2010) 3792–3796, <https://doi.org/10.1016/j.tsf.2010.01.003>.
- [6] F. Meng, Z. Zhang, P. Gao, T. Liu, Y. Boyjoo, D. Guo, Design of composite abrasives and substrate materials for chemical mechanical polishing applications, *Appl. Nanosci.* 10 (2019) 1379–1393, <https://doi.org/10.1007/s13204-019-01211-1>.
- [7] C.-H. Hsieh, C.-Y. Chang, Y.-K. Hsiao, C.-C.-A. Chen, C.-C. Tu, H.-C. Kuo, Recent Advances In Silicon Carbide Chemical Mechanical Polishing Technologies, *Micromachines* 13 (2022), <https://doi.org/10.3390/mi13101752>.
- [8] R. Schmitt, A. Nemning, O. Krainis, R. Korobko, A.I. Frenkel, I. Lubomirsky, S. M. Haile, J.L.M. Rupp, A review of defect structure and chemistry in ceria and its solid solutions, *Chem. Soc. Rev.* 49 (2020) 554–592, <https://doi.org/10.1039/c9cs00588a>.
- [9] J. Seo, A review on chemical and mechanical phenomena at the wafer interface during chemical mechanical planarization, *J. Mater. Res.* 36 (2021) 235–257, <https://doi.org/10.1557/s43578-020-00060-x>.
- [10] J. Kang, W. Feng, D. Guo, K. Chen, S. Gao, J. Jiang, C. Lu, B. Niu, B. Wang, Performance optimization of Ca and Y co-doped CeO_2 -based electrolyte for intermediate-temperature solid oxide fuel cells, *J. Alloys Compd.* 913 (2022), <https://doi.org/10.1016/j.jallcom.2022.165317>.
- [11] H. Jia, J. Hu, H. Chen, J. Wu, X. Tan, S. Sun, Effect of 3.7 at% F doping on the atomic structure and reducibility of $\text{CeO}_2(111)$ surface: A first principles calculation, *Curr. Appl. Phys.* 43 (2022) 9–14, [10.1016/j.cap.2022.08.001](https://doi.org/10.1016/j.cap.2022.08.001).
- [12] Y. Chen, M. Wang, W. Cai, T. Wang, A. Chen, Structural regulation and polishing performance of dendritic mesoporous silica (D-mSiO₂) supported with samarium-doped cerium oxide composites, *Adv. Powder Technol.* 33 (2022), <https://doi.org/10.1016/j.apnt.2022.103595>.
- [13] E. Kim, J. Lee, C. Bae, H. Seok, H.-U. Kim, T. Kim, Effects of trivalent lanthanide (La and Nd) doped ceria abrasives on chemical mechanical polishing, *Powder Technol.* 397 (2022), <https://doi.org/10.1016/j.powtec.2021.11.069>.
- [14] Y. Fan, J. Jiao, L. Zhao, J. Tang, Preparation of lanthanide-doped polystyrene/ CeO_2 abrasives and investigation of slurry stability and photochemical mechanical polishing performance, *Colloid. Surface A* 656 (2023), <https://doi.org/10.1016/j.colsurfa.2022.130508>.
- [15] J. Ma, N. Xu, J. Hu, Y. Luo, Y. Lin, Y. Pu, Doping strategy on properties and chemical mechanical polishing performance of CeO_2 Abrasives: A DFT assisted experimental study, *Appl. Surf. Sci.* 623 (2023), <https://doi.org/10.1016/j.apsusc.2023.156997>.
- [16] X. Han, M. Benkraouda, Z. Zhang, N. Amrane, Oxygen vacancy diffusion and dynamics in Gd-doped CeO_2 : A GGA+U study, *Solid State Commun.* 375 (2023), <https://doi.org/10.1016/j.ssc.2023.115359>.
- [17] Z. Liu, H. Ma, C.C. Sorrell, P. Koshy, B. Wang, J.N. Hart, Enhancement of light absorption and oxygen vacancy formation in CeO_2 by transition metal doping: A DFT study, *Appl. Catal., A* 670 (2024) 10.1016/j.apcata.2023.119544.
- [18] D. Datta, H. Rai, S. Singh, M. Srivastava, R.K. Sharma, N.N. Goswami, Nanoscale tribological aspects of chemical mechanical polishing: A review, *Appl. Surf. Sci.* Adv. 11 (2022), <https://doi.org/10.1016/j.apsadv.2022.100286>.
- [19] A. Chen, J. Long, Z. Li, Y. Chen, Dependency of structural change and polishing efficiency of meso-silica/ceria core/shell composite abrasives on calcination temperatures, *J. Mater. Sci.: Mater. Electron.* 29 (2018) 11466–11477. 10.1007/s10854-018-9239-1.
- [20] A. Chen, J. Long, Z. Li, Y. Chen, Copper chemical mechanical polishing performances of polystyrene/ceria hybrid abrasives with a core/shell structure, *J. Inorg. Organomet. Polym. Mater.* 28 (2018) 1655–1663, <https://doi.org/10.1007/s10904-018-0840-9>.
- [21] J. Murata, Y. Ueno, K. Yodogawa, T. Sugiura, Polymer/ CeO_2 – Fe_3O_4 multicomponent core-shell particles for high-efficiency magnetic-field-assisted

- polishing processes, Int. J. Mach. Tools Manuf. 101 (2016) 28–34, <https://doi.org/10.1016/j.ijmachtools.2015.11.004>.
- [22] A. Chen, W. Wang, X. Ma, Y. Chen, Ceria coated hexagonal mesoporous silica core-shell composite particle abrasives for improved chemical-mechanical planarization performance, J. Porous Mater. 26 (2018) 1005–1015, <https://doi.org/10.1007/s10934-018-0699-8>.
- [23] Z. Kou, C. Wang, W. Zhou, A. Chen, Y. Chen, Trivalent lanthanum and ytterbium doped meso-silica/ceria abrasive systems toward chemical mechanical polishing (CMP) and ultraviolet irradiation-assisted photochemical mechanical polishing (PCMP), Appl. Surf. Sci. 657 (2024), <https://doi.org/10.1016/j.apsusc.2024.159733>.
- [24] C. Qin, Z. Hu, A. Tang, Z. Yang, S. Luo, An efficient material removal rate prediction model for cemented carbide inserts chemical mechanical polishing, Wear 452–453 (2020), <https://doi.org/10.1016/j.wear.2020.203293>.
- [25] Z. Li, L. Jin, Z. Cao, C. Zhang, X. Cao, G. Han, S. Peng, Y. Liu, Development and characterization of a novel RE³⁺ doped Core-shell CeO₂ abrasive system and its glass CMP investigations, Appl. Surf. Sci. 638 (2023), <https://doi.org/10.1016/j.apsusc.2023.158055>.
- [26] M. Li, W. Li, S. Liu, Control of the morphology and chemical properties of carbon spheres prepared from glucose by a hydrothermal method, J. Mater. Res. 27 (2012) 1117–1123, <https://doi.org/10.1557/jmr.2011.447>.
- [27] J.P. Perdew, K. Burke, M. Ernzerhof, Generalized gradient approximation made simple Phys. Rev. Lett. 78 (1997) 1396, <https://doi.org/10.1103/PhysRevLett.78.1396>.
- [28] K. G., F. J., Efficiency of ab-initio total energy calculations for metals and semiconductors using a plane-wave b, Comp. Mater. Sci. 6(1996) 15-50. 10.1016/0927-0256(96)00008-0.
- [29] K. G., F. J., From ultrasoft pseudopotentials to the projector augmented-wave method, Phys. Rev. B 59(1999) 1758-1775.
- [30] B. He, J. Wang, D. Ma, Z. Tian, L. Jiang, Y. Xu, S. Cheng, Interaction of Pd single atoms with different CeO₂ crystal planes: A first-principles study, Appl. Surf. Sci. 433 (2018) 1036–1048, <https://doi.org/10.1016/j.apsusc.2017.10.134>.
- [31] X. Han, N. Amrane, Z. Zhang, M. Benkraouda, Interplay between Gd and oxygen vacancy on the electronic properties and defect chemistry of Gd-doped CeO₂: A DFT + U study, Chem. Phys. 534 (2020), <https://doi.org/10.1016/j.chemphys.2020.110741>.
- [32] Y. Xu, G. Zhao, Q. Wang, Y. Zhan, B. Chen, Study on material removal mechanism of sapphire wafer with CeO₂ coated diamond composite abrasives via green polishing, J. Manuf. Processes 92 (2023) 412–421, <https://doi.org/10.1016/j.jmapro.2023.02.062>.
- [33] Z. Wang, Q. Wu, W. Zhou, F. He, C. Yu, D. Lin, J. Wang, C.T. Liu, Quantitative determination of the lattice constant in high entropy alloys, Scr. Mater. 162 (2019) 468–471, <https://doi.org/10.1016/j.scriptamat.2018.12.022>.
- [34] S. P, Bestimmung der GröÙe und der inneren Struktur von Kolloidteilchen mittels RöÙgenstrahlen, Nachr. Ges. Wiss. Göttingen 1918) 98-100.
- [35] J. Lan, B. Wang, C. Bo, B. Gong, J. Ou, Progress on fabrication and application of activated carbon sphere in recent decade, J. Ind. Eng. Chem. 120 (2023) 47–72, <https://doi.org/10.1016/j.jiec.2022.12.045>.
- [36] H. Wang, J. Shang, Z. Xiao, P. Aprea, S. Hao, Novel construction of carbon bonds in CeO₂@C with efficiently photocatalytic activity, Dyes Pigm. 182 (2020), <https://doi.org/10.1016/j.dyepig.2020.108669>.
- [37] C. Chen, Y. Cui, X. Li, S. Shen, W. Liao, H. You, Novel ceria/graphene oxide composite abrasives for chemical mechanical polishing, Ceram. Int. 50 (2024) 26325–26333, <https://doi.org/10.1016/j.ceramint.2024.03.193>.
- [38] X. Yuan, C. Chen, H. Lei, Z. Zhang, Synthesis, characterization of CeO₂@ZIF-8 composite abrasives and their chemical mechanical polishing behavior on glass substrate, Ceram. Int. 49 (2023) 5189–5198, <https://doi.org/10.1016/j.ceramint.2022.10.037>.
- [39] H. Bairagi, P. Vashishth, R. Narang, S.K. Shukla, B. Mangla, Protection of mild steel from corrosion in an aggressive chloride media through chitosan-CeO₂ nanocomposite: experimental and computational studies, Corros. Commun. (2024), <https://doi.org/10.1016/j.corcom.2023.08.003>.
- [40] T. Wang, Y. Chen, A. Chen, Y. Chen, Development of carbon sphere/ceria (CS/CeO₂) heterostructured particles and their applications to functional abrasives toward photochemical mechanical polishing, Appl. Surf. Sci. 593 (2022), <https://doi.org/10.1016/j.apsusc.2022.153449>.
- [41] D.J. Lee, P.-K. Hsu, Y.-C. Chen, A. Gloter, S.-Y. Chen, Surface and interface mediated magnetism in mesoscopic ceria@carbon core-shell structures, Surf. Interfaces 38 (2023), <https://doi.org/10.1016/j.surfin.2023.102817>.
- [42] Z.-J. Sun, H. Ge, S. Zhu, X.-M. Cao, X. Guo, Z.-H. Xiu, Z.-H. Huang, H. Li, T. Ma, X.-M. Song, Versatile template-free construction of hollow nanostructured CeO₂ induced by functionalized carbon materials, J. Mater. Chem. 7 (2019) 12008–12017, <https://doi.org/10.1039/c9ta0747k>.
- [43] Z.X. Yang, D.W. Ma, X.H. Yu, K. Hermansson, The main factors influencing the O vacancy formation on the Ir doped ceria surface: A DFT+U study, The, Eur. Phys. J. B 77 (2010) 373–380, <https://doi.org/10.1140/epjb/e2010-00295-x>.
- [44] M. Nolan, Charge compensation and ce3+formation in trivalent doping of the CeO₂(110) surface: the key role of dopant ionic radius, J. Phys. Chem. C 115 (2011) 6671–6681, <https://doi.org/10.1021/jp112112u>.
- [45] S. Grieshammer, B.O. Grope, J. Koettgen, M. Martin, A combined DFT + U and Monte Carlo study on rare earth doped ceria, Phys. Chem. Chem. Phys. 16 (2014) 9974–9986, <https://doi.org/10.1039/c3cp54811b>.
- [46] S. Grieshammer, M. Nakayama, M. Martin, Association of defects in doped non-stoichiometric ceria from first principles, Phys. Chem. Chem. Phys. 18 (2016) 3804–3811, <https://doi.org/10.1039/c5cp07537h>.
- [47] Z. Hu, H. Metiu, Effect of dopants on the energy of oxygen-vacancy formation at the surface of ceria: local or global? J. Phys. Chem. C 115 (2011) 17898–17909, <https://doi.org/10.1021/jp205432r>.
- [48] X. Chen, Y. Zhao, Y. Wang, Modeling the effects of particle deformation in chemical mechanical polishing, Appl. Surf. Sci. 258 (2012) 8469–8474, <https://doi.org/10.1016/j.apsusc.2012.04.079>.
- [49] X. Yuan, H. Lei, C. Chen, An ethylenediaminetetraacetic acid (EDTA) surface-functionalized CeO₂ composite abrasives with the effective improvement of the removal rate on glass CMP, Ceram. Int. 50 (2024) 293–305, <https://doi.org/10.1016/j.ceramint.2023.10.103>.
- [50] Y. Chen, R. Long, Polishing behavior of PS/CeO₂ hybrid microspheres with controlled shell thickness on silicon dioxide CMP, Appl. Surf. Sci. 257 (2011) 8679–8685, <https://doi.org/10.1016/j.apsusc.2011.05.047>.
- [51] L. Cook, M, Chemical processes in glass polishing, J. Non-Cryst. Solids 120 (1990) 152–171, [https://doi.org/10.1016/0022-3093\(90\)90200-6](https://doi.org/10.1016/0022-3093(90)90200-6).
- [52] N. Ozawa, M. Ishikawa, M. Nakamura, M. Kubo, Polishing Process Simulation of SiO₂ by CeO₂ Abrasive Grain under Wet Environment, Hyomen Kagaku 33(2012) 351-356. 10/gr8hmj.